Laser surface texturing of alumina/zirconia composite ceramics for potential use in hip joint prosthesis

coatings

MDPI

Article

Laser Surface Texturing of Alumina/Zirconia Composite Ceramics for Potential Use in Hip Joint Prosthesis

Francesco Baino [1,*], Maria Angeles Montealegre [2], Joaquim Minguella-Canela [3] and Chiara Vitale-Brovarone [1]

1 Department of Applied Science and Technology, Politecnico di Torino, Corso Duca degli Abruzzi 24, 10129 Torino, Italy; chiara.vitale@polito.it
2 AIMEN Technology Centre, Relva 27A Torneiros, 36410 Porriño, Spain; mmontealegre@outlook.es
3 Centre CIM, Departament d'Enginyeria Mecànica, Universitat Politècnica de Catalunya, Av. Diagonal, 647, 08028 Barcelona, Spain; joaquim.minguella@upc.edu
* Correspondence: francesco.baino@polito.it; Tel.: +39-011-090-4668

Received: 18 April 2019; Accepted: 5 June 2019; Published: 6 June 2019

Abstract: The use of metal shell to fix an acetabular cup to bone in hip joint prosthesis carries some limitations, including restrictions in prosthetic femur ball diameter and in patient's range of motion. These drawbacks could be ideally overcome by using a monolithic ceramic acetabular cup, but the fixation of such an implant to host bone still remains a challenge. Since porous surfaces are known to promote more bone tissue interlocking compared to smooth materials, in this work the surfaces of sintered alumina/zirconia composite ceramics were treated by a pulsed laser radiation at 1064 nm with a pulse width in the nanosecond range, in order to impart controlled textural patterns. The influence of laser process parameters (e.g., energy per pulse, repetition rate, scanning speed, repetition number, angle of laser beam, and number of cycles) on the roughness and texture orientation was systematically investigated. The obtained surface topographies were inspected by optical and scanning electron microscopy, and the roughness was assessed by contact profilometry. Surface roughness could be modulated in the range of 3 to 30 μm by varying the processing parameters, among which the number of cycles was shown to play a major role. The laser treatment was also successfully adapted and applied to ceramic acetabular cups with a curved profile, thus demonstrating the feasibility of the proposed approach to process real prosthetic components.

Keywords: bioceramics; laser ablation; roughness; composites; hip joint prosthesis; cementless cup; bone

1. Introduction

The hip joint prosthesis has been the most active field of research in prosthetics over the last decades [1]. This high interest was mainly dictated by the increasing demand for such an implant in the elderly due the increment of the aging population worldwide [2]. Both the acetabular component and the femur stem are often fixed to the patient's bone using acrylic cement; however, this approach, despite the ease of execution, suffers from some drawbacks. Firstly, the in-situ cement polymerization reaction is typically associated to a sudden increase of local temperature that can induce bone tissue necrosis. Secondly, the cement is prone to disintegrate over time and produces debris, which may yield implant mobilization and bone necrosis at the operation site in the long term [3]. Therefore, several prosthetic models have been developed in the attempt to overcome the need for acrylic cement while ensuring satisfactory and safe performance of the implant [4–6]. This is particularly challenging if

adopting ceramic-on-ceramic bearings is a goal, given that such combinations are the most favorable in regard to excellent bio-inertness and minimal wear [7].

Cementless ceramic acetabular components were introduced for the first time in total hip arthroplasty in the 1970s, and monolithic ceramic screwed cups were typically combined with cemented femur stems having a ceramic ball head [8]. In 1999, Griss et al. [9] presented the long-term results of alumina screwed cylindrical implants and reported that 24 cases out of 67 underwent surgical revision due to loosening and migration of the acetabular cup. Another 25 cups were still in situ after 22 years of implantation, but all of them were found to have migrated to a certain extent under radiographic investigation.

Gierse et al. [10] also reported an initial or short-term postoperative migration in 35% of the patients receiving this ceramic cup.

Monolithic ceramic screwed cups with a conical shape were also proposed (the so-called Mittelmeier design), but high rates of implant loosening (53% after 12.3 years of postoperative follow-up) were reported [11].

The clinical use of all these screwed ceramic cups was soon stopped due to the above-mentioned postoperative problems and, at present, ceramic-on-ceramic bearing is based on a "modular" concept, i.e., a metal shell is used as a press-fit cementless acetabular component combined with a ceramic insert [12].

In principle, this design style suffers from a major disadvantage compared to monolithic cups, i.e., the inherent minimum thickness of metal shell and insert together, which restricts the use of both small-sized cups and large-diameter femur heads. Furthermore, problems of incorrect positioning (miscentering) of the ceramic insert into the metal shell might occur during surgery.

After a hiatus of about 20 years, the idea of fabricating monolithic ceramic cups able to be somehow anchored to the pelvic bone without using acrylic cement or metal shell was resurrected by Schreiner et al. [13], who pointed out the beneficial effect of surface porosity for allowing osteoconduction. This property was first reported by Forgon et al. [14] who observed bone ingrowth into 500 μm holes drilled in alumina implants. As discussed later by Cornell and Lane [15], osteoconduction can be observed in biomaterials that have a porosity similar to that of bone architecture. In fact, although growth factors, local cytokines, and other biomolecules modulate the process—which also strongly depends on the composition of the implanted material—the three-dimensional (3D) structure of an implant still plays a key role in affecting the host biological responses.

In their study published in 2011, Schreiner et al. [13] evaluated the osteointegration of alumina/zirconia composite cups (BIOLOX delta®, CeramTec, Plochingen, Germany) with a porous outer surface after implantation in a sheep model for 8 and 52 weeks. Stable osteointegration was detected at both time points and the interlocking of bone tissue into the implant pores was claimed to provide a stable fixation of the cup in the presence of low osteointegration rates. Since then, investigations on this material were apparently discontinued; this was probably due to commercial reasons, as other studies proved the role of pores in promoting osteoconduction even in porous or variously rough metallic implants [16], which are easier to process than ceramics and have eventually led to the development and clinical use of trabecular metal in orthopedics and dentistry.

Recently, porous bioactive glass coatings have also been manufactured by sponge replication [17–19] or laser cladding [20,21] on the outer surface of the alumina/zirconia monolithic cup in order to take advantage from both the trabecular bone-like morphology of the coating and the inherent bioactivity of the glass used.

The present study aims at investigating the suitability of laser treatments to impart a controlled surface texture to alumina/zirconia composite ceramics for potential use in the fabrication of acetabular components for hip joint replacement. Laser-based methods have been used in the field of bioceramics to manufacture bioactive non-porous implants with complex (curved) geometry [22–24] and coatings [25,26], but, to the best of the authors' knowledge, their potential suitability for the surface ablation of ceramic acetabular cups has not been reported yet.

2. Materials and Methods

2.1. Manufacturing of Ceramic Samples

In order to proceed to a set of experiments to test the suitability of laser treatments, it was necessary to manufacture a series of alumina/zirconia ceramic samples in the shape of acetabular cups and discs. In order to obtain alumina/zirconia shapes, some different approaches have already been explored. Whilst additive manufacturing has proven to be a suitable procedure for obtaining prosthetic parts with a controlled porosity [27], the approach via subtractive manufacturing technologies [28] is the one that, up to now, yields to the best results if high-load-bearing applications are the major goal.

For the cups required for testing, the raw material utilized was a powder composition of alumina/zirconia in a 75/25 (wt %) ratio, which undertook a process of hydrostatical compression to achieve a minimum consistency level, i.e., brown cylinders of 50 mm diameter and 100 mm of height, as shown in Figure 1a. These brown cylinders were then heat treated in a first pre-sintering process with a total duration of 17 h in an oven with forced air circulation (Hobersal Mod JM 3/16, Hobersal, Caldes de Montbui, Spain). The pre-sintering curve contained a first stop of 2 h at 100 °C to remove humidity and a final stop of 2 h at 1200 °C to achieve further mechanical stability in order to be machined, i.e., green cylinders were obtained.

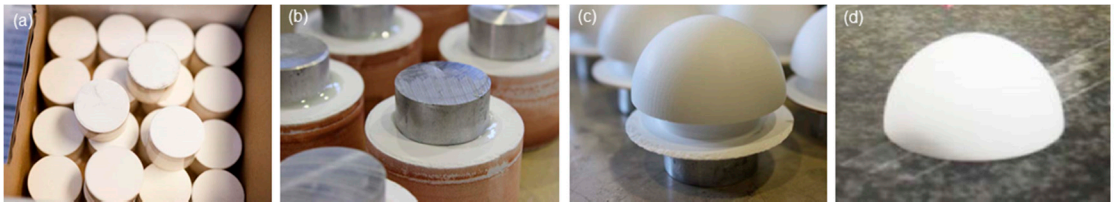

Figure 1. Raw material different stages of transformation during the manufacturing of the cup samples: (**a**) brown cylinders, (**b**) green cylinders fixed to the aluminum support discs, (**c**) green hemispheres before cross-cutting, and (**d**) sintered cups.

The subjection methods utilized for fixing the green cylinders to be machined in the milling center were those described in [29]. In particular, for the machining of the outer surface, a two-component epoxy resin was used to fix each cylinder onto an aluminum disc that was then clamped by the mill clutches, as shown in Figure 1b. Concerning the machining of the inner surface, a specific tailor-made tooling was utilized to hold each of the cylinders already processed in the form of a hemisphere, as per the shape depicted in Figure 1c.

The machining of the outer surface required up to three milling operations (end mill, ball-nose mill, and T-slot cutter operations) whilst the machining of the inner surface required two milling operations (end mill and ball-nose mill operations). Both surfaces' machining processes were performed by a vertical CNC-3 axis milling machine (Milltronics Mod RH20, Milltronics, Waconia, MN, USA). The separation of the semi-processed cylinders (hemispheres) from the aluminum discs was performed by a simple crosscut of the ceramics.

Once machined, the green cups were heat treated in a sintering process with a total duration of 30 h in an oven with forced air circulation (Hobersal Mod JM 3/16, Hobersal, Caldes de Montbui, Spain). The sintering curve contained a 2 h stop at 160 °C that yielded the final mechanical properties, i.e., ceramic cup samples to be utilized in the subsequent steps, as shown in Figure 1d.

The details of the process for obtaining the discs required for testing are fully described in [21]. Comparing with the process for the cups, all steps (hydrostatic pressing, machining, and heat treatments) were analogous, taking into consideration that the dimensions of the initial cylinders were much smaller in the discs' case. Also, the machining operations for the discs were simpler, as they could be undertaken simply via turning operations in a Multitask Centre [21].

2.2. Laser Treatment

Several structured surfaces have been generated on the alumina/zirconia ceramic discs using a Q-switched Nd:YVO4 laser source operating in near infrared (wavelength λ = 1064 nm) (Rofin PowerLine E20, Rofin, Gilching, Germany). This source provides a laser beam with the following characteristics: M2 < 1.2, about 10 ns pulse length, up to 200 kHz repetition rate, and up to 800 μJ energy per pulse. The beam was delivered with a galvoscanner head with 254 mm focal length field optics, providing a spot size of 70 μm full width at half maximum (FWHM) diameter.

The dominant regime during the process was a combination between ablation (primary effect) and melting—this was the result of smart scanning strategies used to irradiate the surface with the laser beam, provided by a Q-switched laser source of high repetition rate and pulse length in the nanosecond range. This laser beam has a Gaussian energy distribution, which means that the higher energy density is concentrated in the middle of the spot (ablative behavior).

The laser source was equipped with scanner heads having galvanometric mirrors, as shown in Figure 2. The treated surface was scanned combining parallel lines and different overlapping angles between the lines in order to produce periodic or random patterns on the surface. Figure 2 shows a scheme of the experimental set-up adopted in this study.

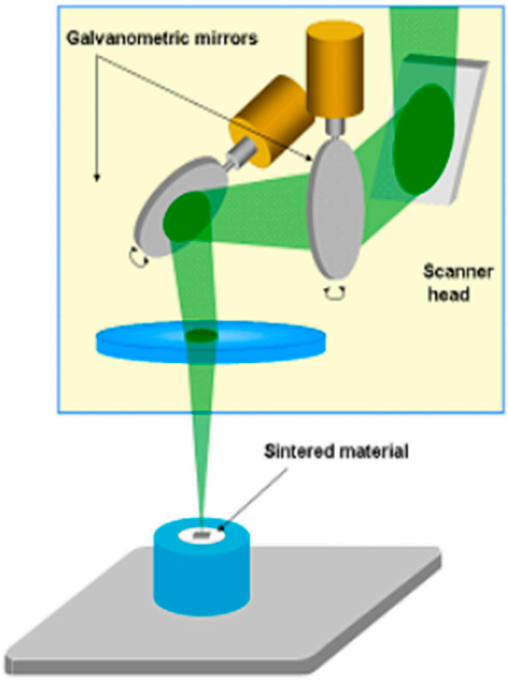

Figure 2. Laser treatment of ceramic surfaces: experimental set-up.

The main processing parameters to take into account in laser surface texturing include the laser wavelength (which is fixed as it depends on the laser source), the energy per pulse (which depends on the supplied power and the repetition rate), the scanning speed, the repetition rate (which is the number of laser pulses emitted in 1 s), the pulse overlapping (which depends on the scanning speed and the repetition rate), the repetition number (which is the number of overlapped scanning layers to generate the final pattern), the number of cycles, and the focal distance (which was fixed on the sample surface).

Before undergoing surface laser treatment, the ceramic discs were embedded in resin, cut, and polished by a diamond paste in order to reproduce the finely polished surface of currently-used real prosthetic components used in clinical applications.

Each scanning layer was generated with parallel lines separated by an interspace of 100 μm. The laser beam scanned the surface using parallel lines to cover the treated area and the various surface

textures were obtained after several repetitions, as shown in Figure 3. The details of the processes are summarized in Table 1.

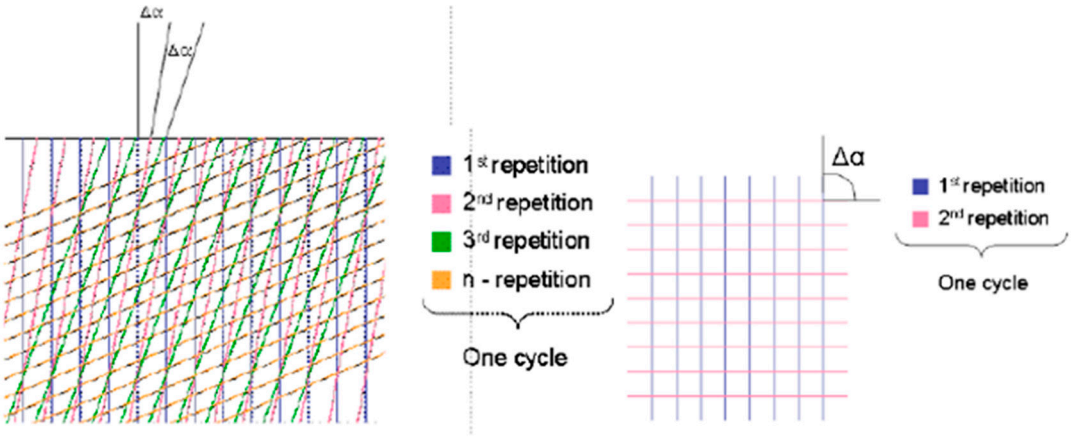

Figure 3. Laser treatment of ceramic surfaces: scheme of the process with different angles (Δα = 20° or 90°).

Table 1. Laser process parameters used to treat the ceramic discs.

Sample Identity	Energy per Pulse (μJ)	Repetition Rate (kHz)	Scanning Speed (mm/s)	Δα (°)	Repetition Number	Cycles
1a	240	60	1000	20	20	1
2a	240	60	1000	20	20	5
1b	240	60	300	20	20	1
2b	240	60	300	20	20	5
1c	240	20	1000	20	20	1
2c	240	20	1000	20	20	5
1d	240	20	300	20	20	1
2d	240	20	300	20	20	5
3d	555	20	300	20	20	1
4a	240	60	300	90	2	1
4b	240	60	300	90	2	2
4c	240	60	300	90	2	3
4d	240	60	300	90	2	4
5	240	60	300	90	2	10

While the application of laser treatment to the surface of flat ceramic discs was relatively easy from a technological viewpoint, adapting this procedure to a ceramic cup was a challenging issue due to the need for scanning a 3D hemispheric geometry. A simple vertical scanning from the 0° position was impossible as the attach angle would vary as much as the distance from the beam focuses to the surface. Of course, there was the same problem if the cup was rotated and treated from the 90° position. In order to tackle this challenge, it was decided to divide the hemispheric cup in sectors to be processed one by one as they were considered almost flat surfaces. In this way, each of these surfaces would not have an excessive attack angle or focal distance variation. Each cup was radially divided in 72 sectors having an angular step size of 5°; four axial divisions were also considered as shown in Figure 4. The first of these divisions was laser-treated from the 90° positions while the rotatory axis turned the ceramic cup of 5° per step. Then, the second and third divisions were processed using a rotatory axis of 45° according to the procedure explained previously. Finally, the ceramic cup was treated from 0° positions in its fourth division without the need for sectors or rotatory axes. Figure 4 shows a scheme of the programmed trajectory to treat the ceramic cups and Figure 5 shows the cup during laser treatment. The process parameters used to obtain a laser-textured cup prototype were the same adopted for the sample 7a.

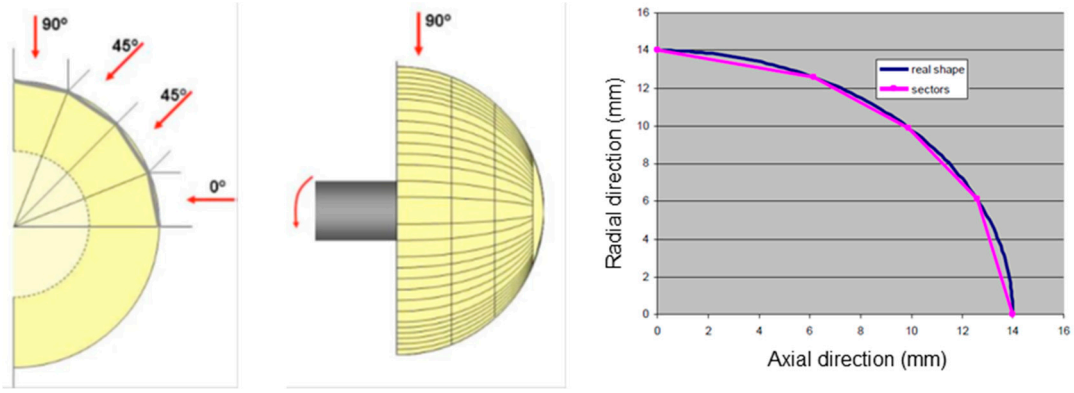

Figure 4. Schemes showing how the ceramic cup was processed by laser treatment.

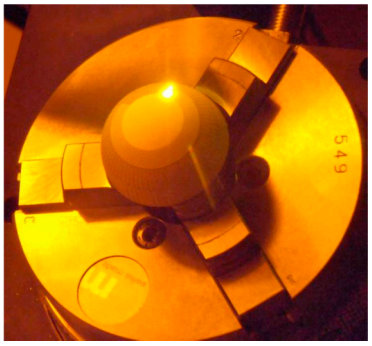

Figure 5. Camera picture showing the real-time laser texturing of the outer surface of the cup.

2.3. Characterization

2.3.1. Microstructure

Phase analysis of the ceramic samples before and after laser treatment was carried out by wide-angle X-ray diffraction (XRD; X'Pert Pro PW3040/60 diffractometer, PANalytical, Eindhoven, The Netherlands) using Cu Kα incident radiation. The XRD pattern was recorded in the 2θ-range of 10°–70° with a step size of 0.2° and a time per step of 0.5 s. Phase analysis and quantification were performed using X'Pert HighScore software (version 2.2b, PANalytical, Eindhoven, The Netherlands) equipped with the PCPDFWIN database. These XRD analyses were performed on solid sintered samples.

2.3.2. Morphology and Composition

Morphological characterization was performed using both optical and scanning electron microscopy (SEM) on selected laser-treated samples. Specifically, an Olympus metallographic optical microscope (Olympus Global, Tokyo, Japan) and a Hitachi FE-4500 field-emission SEM equipment (Hitachi Global, Tokyo, Japan) were used. Compositional analysis was performed by an energy dispersive X-ray spectroscopy (EDS) microprobe attached to the SEM. The samples were sputter-coated with an ultrathin metallic layer prior to undergoing SEM and EDS analyses.

2.3.3. Surface Roughness

Topographical analyses were carried out through the assessment of surface roughness under the ISO 4288 standard [30] using a contact profilometer (Dektak 8, Veeco, Plainview, NY, USA). Six measure lines along the transversal and longitudinal (orthogonal) directions were considered to achieve an average of the roughness value.

Amplitude parameters are the most important and commonly-used parameters to characterize surface topography. They are used to measure the vertical characteristics of the surface deviations. The

arithmetic average height (R_a) is the most universally-used roughness parameter for general quality control. It is defined as the average absolute deviation of the roughness irregularities from the mean line over one sampling length. This parameter is easy to define and measure, and it gives a general description of height variations.

The surface topography can be also described by the root mean square roughness (R_q), which represents the standard deviation of the distribution of surface heights. This parameter is more sensitive than R_a to large deviations from the mean line. The R_q mean line is the line that divides the profile so that the sum of the squares of the deviations of the profile height from it is equal to zero.

R_a and R_q of each sample are expressed as mean ± standard deviation calculated on six values.

3. Results and Discussion

Figure 6 shows the XRD pattern of the sintered ceramic samples. Alumina (Al_2O_3) and tetragonal zirconia (ZrO_2) were detected and quantified in a 76-to-24 wt % ratio, which is consistent with the theoretical expectations and confirms the composite nature of the material.

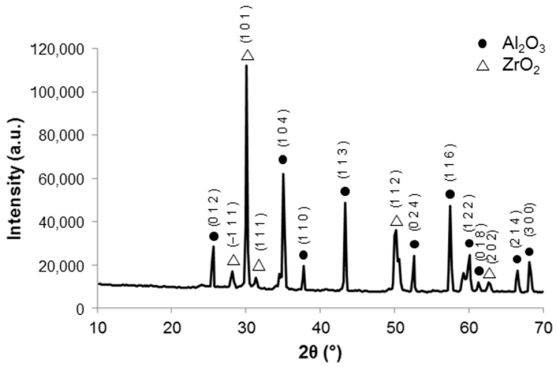

Figure 6. XRD pattern of a sintered ceramic sample.

Figure 7a reports a SEM micrograph on a polished cross-section of the sintered material, where bright inclusions seem to be embedded in a dark matrix. The compositional mapping reported in Figure 7b–d allowed the visualization of the distribution of the elements on the cross-sectional area. The distribution of colors revealed that the dark matrix corresponds to Al_2O_3 and the bright zones can be assigned to ZrO_2. These observations are complementary and consistent with the XRD results shown in Figure 6.

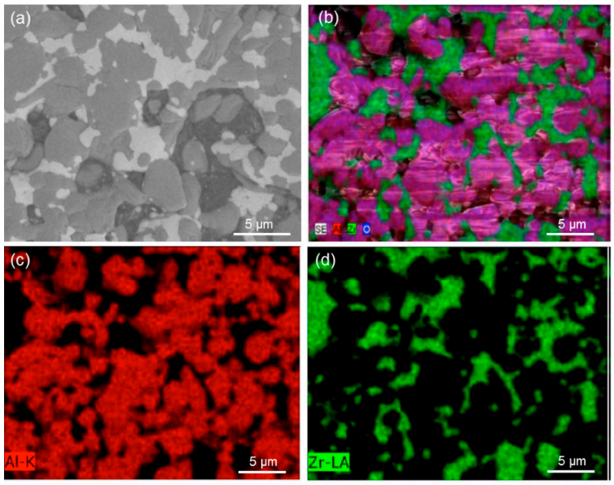

Figure 7. Morphological and compositional analyses of the sintered composite ceramics: (**a**) SEM micrograph and (**b**) compositional map achieved by energy dispersive X-ray spectroscopy (EDS), (**c**,**d**) show the distribution of Al (red) and Zr (green), respectively, with reference to the image (**b**).

Polished ceramic samples were processed by near-infrared laser under different conditions in order to impart different textures to the surface. It was generally observed that the samples acquired a dark color after laser treatment, as shown in Figure 8a. The XRD pattern of laser-treated samples (not shown) revealed the same crystalline phases (alumina and zirconia) that were detected in the original ceramic material, which however exhibited a white color. The only differences between the XRD patterns of as-such and laser-treated ceramics were the lower intensity of the peaks and the noisier pattern in the latter, which were due to the presence of the laser-induced surface roughness.

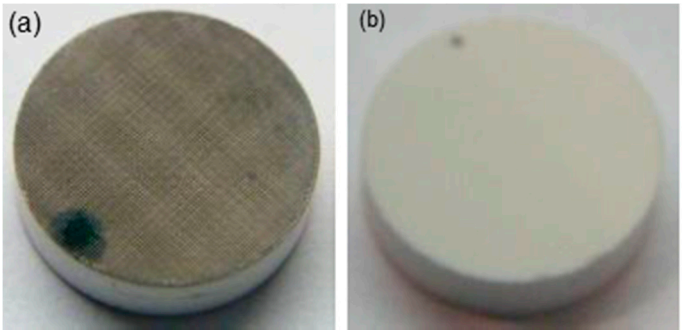

Figure 8. Laser-treated sample (**a**) before and (**b**) after post-treatment in an oven at 700 °C.

The explanation for the darkness of laser-treated samples could be related to oxygen deficiency of zirconia grains. Darkening of this ceramic material is a well-known phenomenon reported in oxygen sensors when they are exposed to reducing atmospheres. Oxygen vacancies promote the formation of stable absorbing defects, i.e., color centers in zirconia when they are irradiated with the laser beam [31,32]. This phenomenon was also confirmed by a simple experiment—after being exposed to an oxidizing atmosphere at 700 °C for 1 h, the darkened disc-shaped samples recovered their natural white color, as shown in Figure 8b.

As reported in Table 2, ceramic samples with no laser treatment exhibited a submicronic surface roughness, which was due to the minimal residual porosity after sintering; this is also consistent with the morphological observation shown in Figure 7a. The roughness profiles were dominated by valleys rather than peaks protruding from the surface, which is a key requirement in clinical applications in order to reduce the risk of wear of the adjacent prosthetic component and/or tissue abrasion [33].

Table 2. Surface roughness parameters of the ceramic samples with different laser-induced textures.

Sample Identity	R_a (μm)	R_q (μm)
As-such ceramic	0.26 ± 0.025	0.39 ± 0.038
1a	4.48 ± 0.47	6.78 ± 0.62
2a	7.25 ± 0.66	8.58 ± 1.00
1b	11.08 ± 0.64	14.10 ± 0.55
2b	31.03 ± 4.91	38.50 ± 5.88
1c	3.38 ± 0.39	4.18 ± 0.39
2c	7.75 ± 0.47	9.28 ± 0.67
1d	3.45 ± 0.29	4.4 ± 0.36
2d	5.48 ± 0.26	6.90 ± 0.26
3d	8.78 ± 1.93	12.18 ± 3.30
4a	3.78 ± 0.68	4.83 ± 0.76
4b	6.55 ± 0.41	8.08 ± 0.46
4c	8.55 ± 1.24	10.28 ± 1.51
4d	9.78 ± 1.04	12.05 ± 0.99
5	18.84 ± 0.28	21.85 ± 0.26
5 after heat treatment	18.66 ± 0.34	21.53 ± 0.37

In general, laser treatments increased the surface roughness (R_a and R_q) of the sintered ceramic samples up to two orders of magnitude depending on the processing conditions, as shown in Table 2. In general, the relatively low standard deviation for the values of roughness suggest a promising reproducibility of the sample and, thus, a good repeatability of the texturing process.

Some more specific considerations about the influence of the different parameters can also be presented. If all the other laser parameters were kept fixed, an increase of the number of cycles increased the roughness due to the higher ablation of the material surface (see comparison of samples 2a and 1a, 2b and 1b, 2c and 1c, as shown in Figure 9, and 2d and 1d). The decrease of the scanning speed increased the overlap between consecutive pulses, thereby involving an increment of the roughness (see comparison of samples 1a and 2b). The variation of the repetition rate seems to have a very limited effect on the surface roughness (comparison between samples 2a and 2c; no significant differences in terms of R_a, minimal differences in terms of R_q). An increase of roughness was also observed with increasing the energy per pulse (sample 3d vs. 1d)

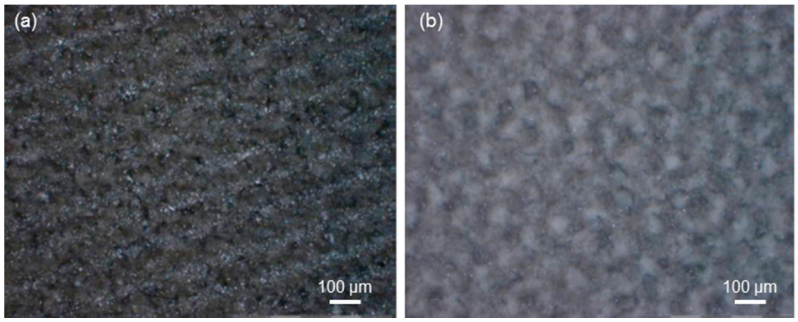

Figure 9. Optical micrographs showing the laser-treated surfaces of (**a**) sample 1c ($\Delta\alpha = 20°$, number of cycles = 1) and (**b**) sample 2c ($\Delta\alpha = 20°$, number of cycles = 5).

The orientation of the surface texture was dictated by the parameter $\Delta\alpha$, as shown in Figure 10. A symmetric textural pattern was obtained as a consequence of using $\Delta\alpha = 90°$, as shown in Figure 10a; on the contrary, a more randomly oriented roughness can be observed in Figure 10b due to an angle of 20° for the laser beam.

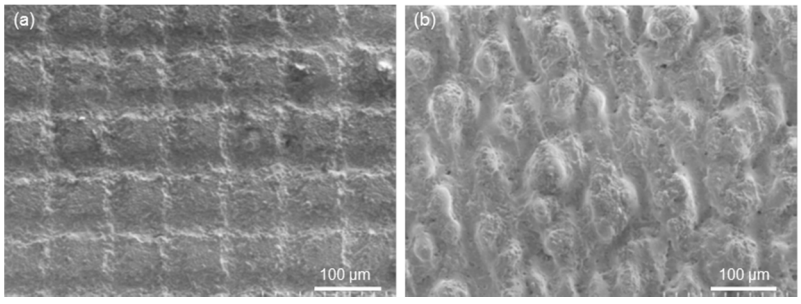

Figure 10. Effect of the parameter $\Delta\alpha$ on the texture orientation: (**a**) sample 4a ($\Delta\alpha = 90°$) and (**b**) sample 1b ($\Delta\alpha = 20°$).

As shown in Figure 11, the orientation of the surface texture was independent of the number of cycles used for the laser treatment and its regularity and periodicity was preserved.

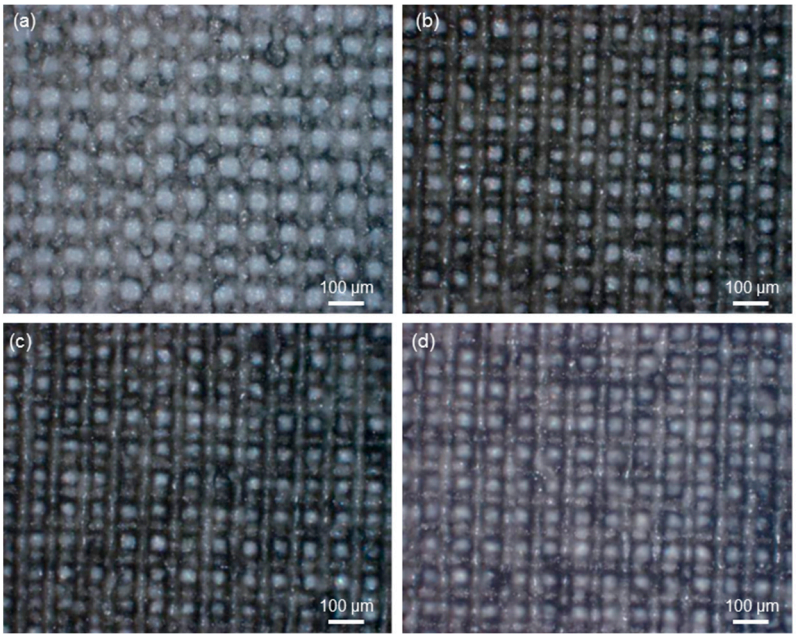

Figure 11. Optical micrographs showing the laser-treated surfaces ($\Delta\alpha = 90°$) of (**a**) sample 4a (number of cycles = 1), (**b**) sample 4b (number of cycles = 2), (**c**) sample 4c (number of cycles = 3), and (**d**) sample 4d (number of cycles = 4).

Building on the numerical results obtained in the experimentation, the significance of the effects of each of the factors investigated on the parameters R_a and R_q were analyzed. As mentioned before, the factors that were the object of study were: energy per pulse (µJ), repetition rate (kHz), scanning speed (mm/s), $\Delta\alpha$ (°), repetition number (units), and number of cycles (units). However, it should be observed that:

- Energy per pulse depends on the repetition rate; which is already in the model.
- In the set of conducted experiments, $\Delta\alpha$ and repetition number were interdependent in the different levels (i.e., in the cases where $\Delta\alpha$ was fixed as 20°, repetition number was always fixed as 20; and in all cases when $\Delta\alpha$ was fixed as 90°, repetition number was always fixed as 2.

Therefore, the screening analysis was performed with the variables repetition rate (kHz), scanning speed (mm/s), $\Delta\alpha$ (°), and number of cycles (units).

Once the conditions were fixed, the data available were analyzed in a frame in the form of a design of experiments (DOE) with four factors, two levels, fractional (2^{4-1} = 8 runs), one block, and no central points. This design, which is presented in Table 3, aimed at screening the significance of the factors analyzed in the overall response for R_a and R_q values.

Table 3. Design of experiments with four factors: A: repetition rate (kHz), B: scanning speed (mm/s), C: $\Delta\alpha$ (°), and D: number of cycles (units). DOE: design of experiments.

DOE Experiment Id	A: Repetition Rate (kHz)	B: Scanning Speed (mm/s)	C: $\Delta\alpha$ (°)	D: Number of Cycles (units)
1	20	300	20	1
2	60	300	20	5
3	20	1000	20	5
4	60	1000	20	1
5	20	300	90	5
6	60	300	90	1
7	20	1000	90	1
8	60	1000	90	5

The data were analyzed by making use of Minitab statistical software (Minitab R18.1, Minitab LLC, State College, PA, USA). The results showed a relatively stronger significance of factor D: number of cycles, compared to the others, as it can be identified in Figure 12a,b. Due to the limited number of experiments in this fractional design, this weak signification would require further investigation in order to decide upon the importance of the response yield. Also, the levels low (number of cycles equal to 1) and high (number of cycles equal to 5) of factor D: number of cycles were not taking into account the entire range of experimentation, but only the one with enough data for the construction of the DOE framework, so further analysis should also address the bigger range.

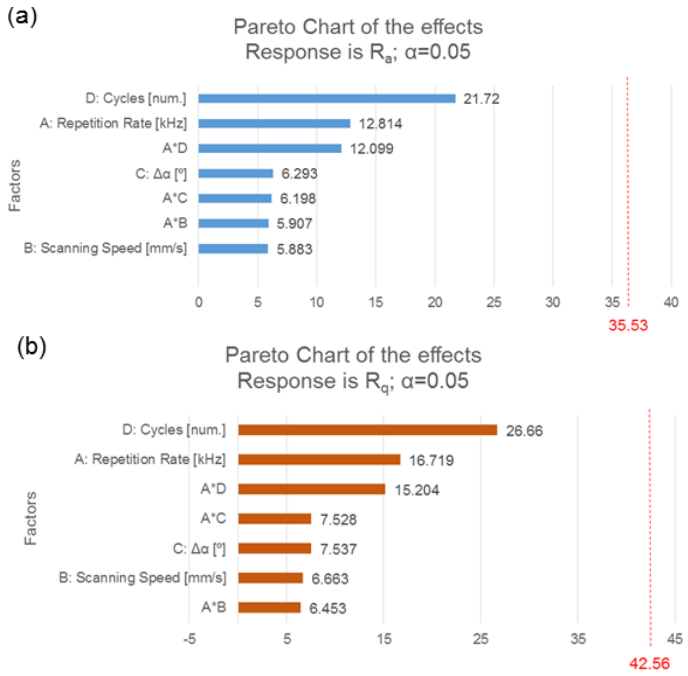

Figure 12. Pareto diagram for the significance of the effects of the variables in the DOE regarding R_a (**a**) and R_q (**b**). Variable D: number of cycles shows a relatively stronger significance than the others in both cases.

For the separated investigation on the influence of variable D: number of cycles to the level of R_a and R_q observed, all available data were used, ranging from a number of cycles equal to 1 to a number of cycles equal to 10. Indeed, a strong linear correlation was found between the number of cycles and the values of R_a and R_q, as revealed by the high value of the coefficients of determination R^2 (above 0.98 in R_a and above 0.96 in R_q), as shown in Figure 13. The resulting linear interpolating functions can be useful from a technological viewpoint in order to predict, at the design stage, the expected roughness depending on laser processing parameters.

Sample 5 exhibited an ordered textural arrangement with regular periodicity of squared "hills" and valleys created by the laser beam, as shown in Figure 14a,b. SEM investigations revealed that a two-level texture can be observed on these samples, i.e., a laser-induced roughness with R_a and R_q values around 20 μm, as shown in Table 2, combined with a finer micro-roughness on the top of the hills, where the ceramic particles were joined and partially melted together during sintering, assuming a quite rounded morphology, as shown in Figure 14c. It is known that nanoparticles can form during processes of laser ablation [34,35]; however, the size of these nanoparticles was shown to typically be within the range of few nanometers, hence they are too small to affect the quality of the surface texture at the scale investigated in the present study. The hierarchical roughness of the samples is expected to be highly favorable to promote osteointegration of the ceramic implants. In fact, the surface roughness due to laser ablation is comparable to the size of human osteoblastic cells, which exhibit a typical diameter within 15–30 μm [36] and can then potentially enter the valleys created by the laser,

thereby leading to new bone tissue interlocking within the implant surface. Furthermore, the fine roughness on the top of the hills could also play a role in promoting bone cell behavior towards paths of osteogenesis and self-repair. Textural properties of implant surfaces are known to greatly influence cell responses in vitro and in vivo [37]. The early studies carried out by Schwartz and Boyan [38] gave a first evidence that osteoblasts attach and spread preferably on implant surfaces with a diffused micrometric roughness. The micrometric and nanometric peaks and valleys of implant surfaces were shown to affect the organization of bone cell cytoskeleton and the intracellular transduction signaling pathways, thus emphasizing the bone regenerative capacity [39,40].

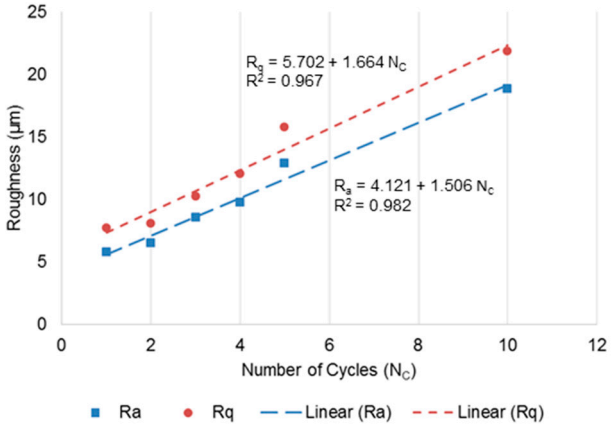

Figure 13. Relationship between surface roughness (R_a and R_q) and number of cycles used during the laser treatment.

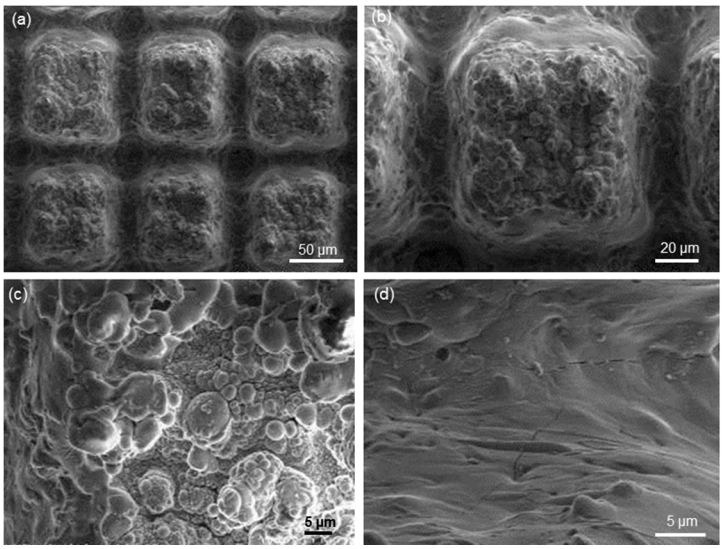

Figure 14. SEM micrographs of sample 5: (**a**) general view and (**b**) detail of the surface texture, (**c**) top surface of a hill and (**d**) detail of the area between two adjacent hills.

Comparison of Figure 14c and d reveal the morphological difference that exists between the top of the hills and the bottom of the laser-created valleys; specifically, Figure 14d shows that melting of the ceramic surfaces produces small cracks in the material as a consequence of the high cooling rate.

As shown in Table 2, the heat post-treatment carried out to eliminate the dark color of the samples caused no significant alteration in the values of R_a and R_q.

A laser-textured prototype of the ceramic cup with square-shaped roughness was successfully obtained, as shown in Figure 15. The laser parameters used to process sample 5 were adopted for this purpose, under the appropriate technological optimization. This choice was based on the values of

roughness reported in Table 2; except for sample 5, all the other laser-textured specimens had a surface roughness above (sample 2b) or below (all the other cases) the typical size range of osteoblastic cells (15–30 μm). Also, in the case of the surface-textured cup, a heat treatment in oxidizing atmosphere was suitable to recover the original white appearance of the cup, as shown in Figure 15b.

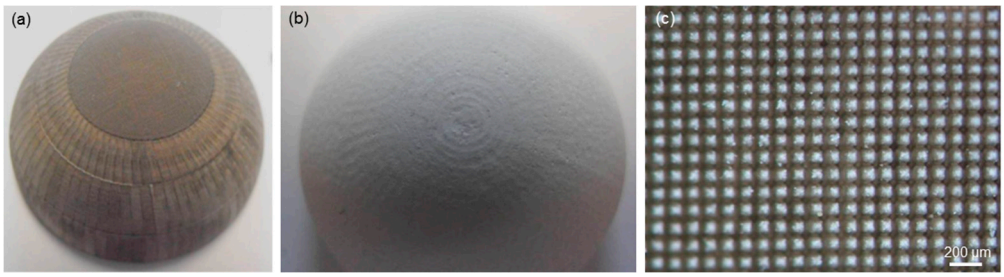

Figure 15. Laser-textured ceramic cup: (**a**) sample after laser treatment, (**b**) sample after thermal treatment in an oven at 700 °C, (**c**) optical micrograph of the surface.

4. Conclusions

In this work, different surface textures were imparted to alumina/zirconia ceramic samples by applying infrared laser ablation strategies. Surface roughness could be modulated in the range of 3 to 30 μm by varying the laser process parameters (e.g., number of cycles, scanning speed, energy per pulse). In general, the roughness increased with (i) increasing number of cycles due to the higher ablation of the material, (ii) decreasing scanning speed, or (iii) increasing the energy per pulse. Critical analysis based on DOE suggests the relatively stronger significance of the number of cycles compared to the other factors. Furthermore, highly-arranged or random-like textures could be obtained depending on the variation of the laser process angle. Morphological investigations revealed a hierarchical texture formed by a laser-induced roughness combined with a finer micro-roughness deriving from the sintering process of the ceramic bodies. The method proposed for laser surface texturing of flat ceramic samples was properly adapted for application on real acetabular cups for hip joint prosthesis, and a prototype was successfully obtained. The produced surface roughness is expected to be suitable for promoting bone tissue in-growth and interlocking in acetabular prosthetic implants; future in vivo studies will allow elucidating if a renaissance of surface-textured cementless monolithic ceramic cups is actually possible.

Author Contributions: Conceptualization, F.B., J.M.-C., M.A.M. and C.V.-B.; Methodology, F.B., J.M.-C., M.A.M. and C.V.-B.; Software, F.B., J.M.-C. and M.A.M.; Validation, C.V.-B.; Formal Analysis, F.B.; Investigation, F.B., J.M.-C., M.A.M. and C.V.-B.; Resources, F.B., J.M.-C., M.A.M. and C.V.-B.; Data Curation, F.B. and M.A.M.; Writing—Original Draft Preparation, F.B. and J.M.-C.; Writing—Review and Editing, F.B., J.M.-C., M.A.M. and C.V.-B.; Visualization, F.B. and J.M.-C.; Supervision, C.V.-B.; Project Administration, C.V.-B. and J.M.-C.; Funding Acquisition, C.V.-B. and J.M.-C.

Funding: This research was funded by the European Commission, Research Executive Agency, EUFP7/2007-2013 SME-2011-1, Specific Programme "Capacities": Research for the benefit of SMEs (BSG-SME), under grant agreement no. 286548 ("Monoblock acetabular cup with trabecular-like coating"—MATCh project).

Conflicts of Interest: The authors declare no conflict of interest. The funders had no role in the design of the study; in the collection, analyses, or interpretation of data; in the writing of the manuscript, or in the decision to publish the results.

References

1. López-López, J.A.; Humphriss, R.L.; Beswick, A.D.; Thom, H.H.Z.; Hunt, L.P.; Burston, A.; Fawsitt, C.G.; Hollingworth, W.; Higgins, J.P.T.; Welton, N.J.; et al. Choice of implant combinations in total hip replacement: Systematic review and network meta-analysis. *BMJ* **2017**, *359*, 4651. [CrossRef] [PubMed]
2. Clegg, A.; Young, J.; Iliffe, S.; Rikkert, M.O.; Rockwood, K. Frailty in elderly people. *Lancet* **2013**, *381*, 752–762. [CrossRef]

3. Edwards, L.D.; Levin, S. Complications from total hip replacement with the use of acrylic cement. *Health Serv. Rep.* **1973**, *88*, 857–867. [CrossRef] [PubMed]
4. Latham, B.; Goswami, T. Effect of geometric parameters in the design of hip implants-paper IV. *Mater. Des.* **2004**, *25*, 715–722. [CrossRef]
5. Sargeant, A.; Goswami, T. Hip implants: Paper V. Physiological effects. *Mater. Des.* **2006**, *27*, 287–307. [CrossRef]
6. Kharmanda, G. Reliability analysis for cementless hip prosthesis using a new optimized formulation of yield stress against elasticity modulus relationship. *Mater. Des.* **2015**, *65*, 496–504. [CrossRef]
7. Rahaman, M.N.; Yao, A.; Sonny Bal, B.; Garino, J.P.; Ries, N.D. Ceramics for prosthetic hip and knee joint replacement. *J. Am. Ceram. Soc.* **2007**, *90*, 1965–1988. [CrossRef]
8. O'Leary, J.F.; Mallory, T.H.; Kraus, T.J.; Lombardi, A.V., Jr.; Lye, C.L. Mittelmeier ceramic total hip arthroplasty. A retrospective study. *J. Arthroplast.* **1988**, *3*, 87–96. [CrossRef]
9. Griss, P.; Claus, A.; Scheller, G. Analyse Unserer Erfahrungen Mit Keramik/Keramik-Huftendoprothesen der Ersten Generation. In *Reliability and Long-Term Results of Ceramics in Orthopaedics*; Sedel, L., Willmann, G., Eds.; Thieme: Stuttgart, Germany, 1999; pp. 43–47.
10. Gierse, H.; Maaz, B.; Hofer, C.; Gruner, S. The ceramic cup type Lindenhof. Results 10–14 years after implantation. *Arch. Orthop. Trauma Surg.* **1996**, *115*, 167–170. [CrossRef]
11. Garcia-Cimbrelo, E.; Martinez-Sayanes, J.M.; Minuesa, A.; Munuera, L. Mittelmeier ceramic-ceramic prosthesis after 10 years. *J. Arthroplast.* **1996**, *11*, 773–778. [CrossRef]
12. Rosner, B.I.; Postak, P.D.; Greenwald, A.S. Cup/liner conformity of modular acetabular designs. *Orthop. Trans.* **1995**, *19*, 469–470.
13. Schreiner, U.; Schulze, A.; Scheller, G.; Apruzzese, C.; Schwarz, M.L. Osseointegration of ceramic cement-free acetabular cups. *Z. Orthop. Unfallchir.* **2011**, *150*, 32–39. [CrossRef] [PubMed]
14. Forgon, M.; Mammel, E.; Trombitas, K.; Kacsalova, L.; Draveczki, I. Morphological investigations of a porous aluminium oxide ceramic and the consequences for clinical application. *Arch. Orthop. Trauma Surg.* **1987**, *106*, 385–389. [CrossRef] [PubMed]
15. Cornell, N.C.; Lane, J.M. Current understanding of osteoconduction in bone regeneration. *Clin. Orthop.* **1998**, *355*, 267–273. [CrossRef] [PubMed]
16. Spriano, S.; Yamaguchi, S.; Baino, F.; Ferraris, S. A critical review of multifunctional titanium surfaces: New frontiers for improving osseointegration and host response, avoiding bacteria contamination. *Acta Biomater.* **2018**, *79*, 1–22. [CrossRef]
17. Baino, F.; Minguella, J.; Kirk, N.; Montealegre, M.A.; Fiaschi, C.; Korkusuz, F.; Orlygsson, G.; Vitale-Brovarone, C. Novel full-ceramic monoblock acetabular cup with a bioactive trabecular coating: Design, fabrication and characterization. *Ceram. Int.* **2016**, *42*, 6833–6845. [CrossRef]
18. Baino, F.; Vitale-Brovarone, C. Trabecular coating on curved alumina substrates using a novel bioactive and strong glass-ceramic. *Biomed. Glasses* **2015**, *1*, 31–40. [CrossRef]
19. Baino, F.; Tallia, F.; Novajra, G.; Minguella-Canela, J.; Montealegre, M.; Korkusuz, F.; Vitale-Brovarone, C. Novel Bone-Like Porous Glass Coatings on Al_2O_3 Prosthetic Substrates. *Key Eng. Mater.* **2014**, *631*, 236–240. [CrossRef]
20. Baino, F.; Montealegre, M.A.; Orlygsson, G.; Novajra, G.; Vitale-Brovarone, C. Bioactive glass coatings fabricated by laser cladding on ceramic acetabular cups: A proof-of-concept study. *J. Mater. Sci.* **2017**, *52*, 9115–9128. [CrossRef]
21. Baino, F.; Minguella-Canela, J.; Korkusuz, F.; Korkusuz, P.; Kankılıç, B.; Montealegre, M.A.; De los Santos-López, M.A.; Vitale-Brovarone, C. In vitro assessment of bioactive glass coatings on alumina/zirconia composite implants for potential use in prosthetic application. *Int. J. Mol. Sci.* **2019**, *20*, 722–737. [CrossRef]
22. Comesaña, R.; Lusquiños, F.; Del Val, J.; Malot, T.; López-Álvarez, M.; Riveiro, A.; Quintero, F.; Boutinguiza, M.; Aubry, P.; De Carlos, A.; et al. Calcium phosphate grafts produced by rapid prototyping based on laser cladding. *J. Eur. Ceram. Soc.* **2011**, *31*, 29–41. [CrossRef]
23. Comesaña, R.; Lusquiños, F.; Del Val, J.; López-Álvarez, M.; Quintero, F.; Riveiro, A.; Boutinguiza, M.; De Carlos, A.; Jones, J.R.; Hill, R.G.; et al. Three-dimensional bioactive glass implants fabricated by rapid prototyping based on CO_2 laser cladding. *Acta Biomater.* **2011**, *7*, 3476–3487. [CrossRef] [PubMed]

24. Del Val, J.; López-Cancelos, R.; Riveiro, A.; Badaoui, A.; Lusquiños, F.; Quintero, F.; Comesaña, R.; Boutinguiza, M.; Pou, J. On the fabrication of bioactive glass implants for bone regeneration by laser assisted rapid prototyping based on laser cladding. *Ceram. Int.* **2016**, *42*, 2021–2035. [CrossRef]
25. Lusquiños, F.; Pou, J.; Boutinguiza, M.; Quintero, F.; Soto, R.; León, B.; Pérez-Amor, M. Main characteristics of calcium phosphate coatings obtained by laser cladding. *Appl. Surf. Sci.* **2005**, *247*, 486–492. [CrossRef]
26. Comesaña, R.; Quintero, F.; Lusquiños, F.; Pascual, M.J.; Boutinguiza, M.; Durán, A.; Pou, J. Laser cladding of bioactive glass coatings. *Acta Biomater.* **2010**, *6*, 953–961. [CrossRef] [PubMed]
27. Minguella-Canela, J.; Villegas, M.; Poll, B.; Tena, G.; Ginebra, M.P. Automatic casting of advanced technical ceramic parts via open source high resolution 3D printing machines. *Key Eng. Mater.* **2014**, *631*, 269–274. [CrossRef]
28. Ayats, J.R.G.; Canela, J.M. Development of a methodology for the materialisation of ceramic rapid prototypes based on substractive methods. *Arch. Mater. Sci.* **2007**, *28*, 9–14.
29. Minguella-Canela, J.; Cuiñas, D.; Rodríguez, J.V.; Vivancos, J. Advanced manufacturing of ceramics for biomedical applications: Subjection methods for biocompatible materials. *Procedia Eng.* **2013**, *63*, 218–224. [CrossRef]
30. *Geometrical Product Specifications (GPS)—Surface Texture: Profile Method—Rules and Procedures for the Assessment of Surface Texture*; ISO 4288; International Organization for Standardization: Geneva, Switzerland, 1996.
31. Orera, V.M.; Merino, R.I.; Chen, Y.; Cases, R.; Alonso, P.J. Intrinsic electron and hole defects in stabilized zirconia single crystals. *Phys. Rev. B* **1990**, *42*, 9782–9789. [CrossRef]
32. Orera, V.M.; Merino, R.I.; Chen, Y.; Cases, R.; Alonso, P.J. Electron and hole trapped defects produced by thermo-reduction or irradiation in stabilized zirconia. *Radiat. Eff. Defects. Solids* **1991**, *119*, 907–912. [CrossRef]
33. Baino, F.; Gautier di Confiengo, G.; Faga, M.G. Fabrication and morphological characterization of glass-ceramic orbital implants. *Int. J. Appl. Ceram. Technol.* **2018**, *15*, 884–891. [CrossRef]
34. Semaltianos, N.G. Nanoparticles by laser ablation. *Crit. Rev. Solid State Mater. Sci.* **2010**, *35*, 105–124. [CrossRef]
35. Kim, M.; Osone, S.; Kim, T.; Higashi, H.; Seto, T. Synthesis of nanoparticles by laser ablation: A review. *KONA Powder Part. J.* **2017**, *34*, 80–90. [CrossRef]
36. Reznikov, N.; Shahar, R.; Weiner, S. Bone hierarchical structure in three dimensions. *Acta Biomater.* **2014**, *10*, 3815–3826. [CrossRef] [PubMed]
37. Feller, L.; Jadwat, Y.; Khammissa, R.A.G.; Meyerov, R.; Schechter, I.; Lemmer, J. Cellular responses evoked by different surface characteristics of intraosseous Ti implants. *BioMed Res. Int.* **2015**, *2015*, 171945. [CrossRef] [PubMed]
38. Schwartz, Z.; Boyan, B.D. Underlying mechanisms at the bone-biomaterial interface. *J. Cell. Biochem.* **1994**, *56*, 340–347. [CrossRef] [PubMed]
39. Qu, Z.; Rausch-Fan, X.; Wieland, M.; Matejka, M.; Schedle, A. The initial attachment and subsequent behavior regulation of osteoblasts by dental implant surface modification. *J. Biomed. Mater. Res. A* **2007**, *82*, 658–668. [CrossRef]
40. Anselme, K.; Davidson, P.; Popa, A.M.; Giazzon, M.; Liley, M.; Ploux, L. The interactions of cells and bacteria with surfaces structured at the nanometer scale. *Acta Biomater.* **2010**, *6*, 3824–12846. [CrossRef]